



# Highly efficient visible-light-driven mesoporous graphitic carbon nitride/ZnO nanocomposite photocatalysts

Shukun Le, Tingshun Jiang\*, Yiwen Li, Qian Zhao, Yingying Li, Weibing Fang, Ming Gong

School of Chemistry and Chemical Engineering, Jiangsu University, Zhenjiang 212013, Jiangsu, China



## ARTICLE INFO

### Article history:

Received 17 May 2016

Received in revised form 16 July 2016

Accepted 18 July 2016

Available online 19 July 2016

### Keywords:

Mesoporous graphitic carbon nitride

Zinc oxide

Visible light photocatalysis

Heterostructure

## ABSTRACT

In order to develop highly efficient visible-light induced photocatalysts, the zinc oxide (ZnO) hybridized with mesoporous graphitic carbon nitride (mpg-C<sub>3</sub>N<sub>4</sub>) nanocomposite photocatalysts (mpg-C<sub>3</sub>N<sub>4</sub>/ZnO) were synthesized through simple one-step calcination in this paper. The physicochemical properties of the synthesized samples were characterized by X-ray diffraction (XRD), Fourier transform infrared spectroscopy (FT-IR), scanning electron microscopy (SEM), transmission electron microscopy (TEM), high-resolution transmission electron microscopy (HRTEM), N<sub>2</sub> physical adsorption, UV-vis diffuse reflectance spectra (DRS), and photoluminescence spectra (PL). Subsequently, the photocatalytic performance of mpg-C<sub>3</sub>N<sub>4</sub>/ZnO was evaluated by photocatalytic degradation of methyl orange (MO) aqueous solution under visible-light irradiation. The photocatalytic activities of the resultant mpg-C<sub>3</sub>N<sub>4</sub>/ZnO nanocomposites were enhanced outstandingly and much higher than that of pure mpg-C<sub>3</sub>N<sub>4</sub> and ZnO. The improved photocatalytic activities of the mpg-C<sub>3</sub>N<sub>4</sub>/ZnO nanocomposites were ascribed to the exaltation of the separation efficiency of photoinduced electron-hole pairs, resulting from the heterojunction established between the interfaces of mpg-C<sub>3</sub>N<sub>4</sub> and ZnO.

© 2016 Elsevier B.V. All rights reserved.

## 1. Introduction

Recently, photocatalytic degradation of harmful pollutants in water has received much attention due to increasing environmental problems. It shows a remarkable ability to decompose the pollutants into harmless substances directly from the contaminant source under sunlight irradiation [1,2]. In spite of the great development and progress in this field, various efforts have been made aiming for large-scale industrial application of photocatalysts in daily human life. TiO<sub>2</sub>-based photocatalysts have been the most popular and a lot of progress has been achieved [3–5]. However, due to the fact that TiO<sub>2</sub> has broad bandgaps and absorb only small fractions of sunlight energy, the use of TiO<sub>2</sub> is limited by its negligible activity under visible light irradiation [6,7]. In order to achieve practical use of photocatalysts, it is urgent to develop highly efficient visible-light induced photocatalysts to meet the high requirements of future environmental purification under visible light illumination.

ZnO is believed to be one of the most widely and deeply studied oxide semiconductors due to its suitable characteristics, such

as the superiority of valuable optical and electronic properties, low cost, and nontoxicity over other kinds of semiconductor materials [8–10]. However, the most fatal drawbacks of ZnO stems from its wide band gap which requires expensive UV light for activation thereby limiting its catalytic efficiency under visible portion of solar spectrum [11]. In addition, undesired photoinduced electron-hole pairs recombination which dominates in the absence of electron acceptor or donor represents the major loss of energy results in the low quantum yield for any photocatalytic reactions [12]. Thus, development of new approaches to modulate the electronic band gap structure of ZnO for visible light response with robust interfacial charge carrier transfer process would be of great interest from the stand point of its practical and widespread use. In order to utilize wide spectrum of incident photon energies, many strategies are developed to tailor the band gap absorption to visible region like metal/nonmetal ion doping [13–17], codoping with foreign ions [18–22], noble metal deposition [23–27] and sensitization by inorganic complexes or organic dyes [28–32]. Among these several methods, incorporation of nonmetallic elements (e.g., C, S, and N) into ZnO matrix has drawn significant attention because of its ability to modify the surface-electronic properties that favors efficient photocatalysis [33]. Since ZnO alone does not absorb visible light, non-metal incorporation helps to reduce the band gap for wide-band-gap metal oxides and extend visible region absorption [34].

\* Corresponding author.

E-mail addresses: [tshjiang@ujs.edu.cn](mailto:tshjiang@ujs.edu.cn), [qianzhao@ujs.edu.cn](mailto:qianzhao@ujs.edu.cn) (T. Jiang).

Another efficient approach is coupling with other materials so as to build a heterojunction structure at the interface to enhance the separation efficiency of photogenerated electron-hole pairs during the photocatalytic process.

As a typical metal free inorganic semiconductor, graphitic carbon nitride ( $\text{g-C}_3\text{N}_4$ ) has attracted extensive attention for pollutant degradation [35],  $\text{H}_2$  generation [36–38] and  $\text{CO}_2$  [39,40] reduction. It is well-known that the smallest direct band gap of  $\text{g-C}_3\text{N}_4$  is about 2.7 eV, which allows a maximal light absorption in the visible-light region (400–460 nm) [41]. Furthermore, the CB minimum of  $\text{g-C}_3\text{N}_4$  is extremely negative, so photogenerated electrons should have high reduction ability. However, the photocatalytic efficiency of the pure  $\text{g-C}_3\text{N}_4$  is limited by the high recombination rate of its photogenerated electron-hole pairs [42]. Accordingly, extending light absorption of  $\text{g-C}_3\text{N}_4$  up to a large portion of the available solar energy becomes very necessary. For this purpose, many methods have been proposed to improve the photocatalytic activity of  $\text{g-C}_3\text{N}_4$  under visible light irradiation. Recently, mesoporous  $\text{g-C}_3\text{N}_4$  ( $\text{mpg-C}_3\text{N}_4$ ) has been successfully prepared via templating methods including soft-templating and hard-templating methods [43–46]. As a photocatalyst, compared with the bulk  $\text{g-C}_3\text{N}_4$ ,  $\text{mpg-C}_3\text{N}_4$  exhibited superior physicochemical properties, such as controllable morphology, tunable pore diameter, higher surface area, and a larger number of active sites on the surface, which can show potentiality in an even wide range of application [47–49].

As described above, one of the techniques for increasing the separation efficiency of photogenerated electron-hole pairs is to form a composite photocatalyst using two kinds of semiconductors. Suitable matching of the band levels of the conduction and valence bands in the two semiconductors offers appropriate driving forces to separate and transfer photogenerated electron-hole pairs [50]. Many studies have confirmed that  $\text{g-C}_3\text{N}_4$  is a good candidate for synthesizing semiconductor heterojunctions with higher photocatalytic activity [51]. As is known to all,  $\text{ZnO}$  is the UV-responsive photocatalyst and  $\text{g-C}_3\text{N}_4$  is the visible-light-driven photocatalyst, after the polymeric  $\text{g-C}_3\text{N}_4$  photocatalyst is combined with  $\text{ZnO}$ , the obtained  $\text{g-C}_3\text{N}_4/\text{ZnO}$  composite may be a promising candidate for efficient photocatalytic activity under visible-light irradiation. Recently, the combination of  $\text{g-C}_3\text{N}_4$  and  $\text{ZnO}$  into a heterostructure presents a feasible and inspiring route to attain an improved charge separation in the electron transfer process. There is a report on the photocatalytic activity for the methyl blue degradation of  $\text{g-C}_3\text{N}_4$ -hybridized  $\text{ZnO}$  photocatalyst fabricated by a twostep chemisorption method [52]. Liu et al. reported the synthesis of  $\text{ZnO}/\text{C}_3\text{N}_4$  photocatalysts through a ball milling method, which resulted in higher photoactivity than that of single-phase  $\text{C}_3\text{N}_4$  [53]. Chen et al. synthesized the core-shell structured  $\text{ZnO}@\text{mpg-C}_3\text{N}_4$  and  $\text{ZnO}/\text{mpg-C}_3\text{N}_4$  composite photocatalysts and found that these composite photocatalysts exhibited high photocatalytic activity under visible light irradiation [54,55]. Nevertheless, seldom attention has been paid to the photocatalytic mechanism of  $\text{mpg-C}_3\text{N}_4/\text{ZnO}$ -catalyzed photodegradation under visible light, which has remained unclear to date.

In this paper, novel  $\text{mpg-C}_3\text{N}_4/\text{ZnO}$  hybrid photocatalysts were prepared by means of a facile calcination approach with the use of commercially available melamine and zinc nitrate as precursors combined with hard-templating method. A series of composites with different weight percentages of  $\text{mpg-C}_3\text{N}_4$  were prepared by simply adjusting the ratio of the precursors, exhibiting enhanced optical property and photocatalytic activity. Methyl orange (MO) dye was chosen as a model pollutant to evaluate the photocatalytic activity of the  $\text{mpg-C}_3\text{N}_4/\text{ZnO}$  hybrid under visible-light irradiation (>440 nm), and the optimal weight fraction of  $\text{mpg-C}_3\text{N}_4$  was determined. In addition, the possible photocatalytic mechanism of  $\text{mpg-C}_3\text{N}_4/\text{ZnO}$  photocatalysis is discussed based on radical trapping and hydroxyl radical detection experiments, and a photo-

toluminescence (PL) technique. The facile preparation process, low cost, and the uniform hybridization make the synthesized nanocomposites show great potential in the fields of sustainable energy and environment.

## 2. Experimental

### 2.1. Materials

The chemicals used in this work, melamine, zinc nitrate, hydrochloric acid, sulfuric acid, hydrofluoric acid, tetraethyl orthosilicate, were purchased from Medicines Group. Copolymers P123 was purchased from Aldrich Company, and methyl orange (MO) was commercially available from Beijing Dye Processing. All chemical reagents in this study were of analytical grade. SBA-15 was prepared using P123 as a template and tetraethyl orthosilicate as silicon source according to our previous publication [56].

### 2.2. Synthesis of $\text{mpg-C}_3\text{N}_4/\text{ZnO}$ nanocomposites

Typically, 4 g of melamine, 0.15 mL concentrated sulfuric acid and 2 g of SBA-15 were added into deionized water to obtain a suspension. Then, the suspension was sonicated for 30 min, and uniformly stirred for 6 h at 70 °C. Heated and stirred at 100 °C and different amounts of zinc nitrate were added. After stirring for 8 h at 100 °C until the water was removed and a white solid was obtained. The solid was grounded, transferred into a tube furnace, and heated to 550 °C at a heating rate 2 °C/min under  $\text{N}_2$  flow and kept at 550 °C for 4 h. After cooling to room temperature, the calcined sample was impregnated with 5 wt% hydrofluoric acid at room temperature for 24 h to remove the SBA-15 template. After that, the sample was washed repeatedly with deionized water, and dried at 60 °C for 12 h in an oven. Finally, a powder was obtained. According to the above manner, a series of  $\text{mpg-C}_3\text{N}_4/\text{ZnO}$  composites with different contents of  $\text{mpg-C}_3\text{N}_4$  were labeled as  $\text{mpg-C}_3\text{N}_4/\text{ZnO-x}$  for simplicity, where x represented the  $\text{mpg-C}_3\text{N}_4$  weight percent in the composites. For a comparative study, the pure  $\text{mpg-C}_3\text{N}_4$  and  $\text{ZnO}$  were prepared via the same route, denoted as  $\text{mpg-C}_3\text{N}_4$  and  $\text{ZnO}$ .

### 2.3. Catalyst characterization

Powder X-ray diffraction (XRD) was carried out with a Japan Shimadzu XRD-6100Lab X-ray diffractometer ( $\text{CuK}\alpha$ , 40 kV, 40 mA), with radiation between 5–80°, and with a scan rate of 4°/min. Fourier transform infrared (FT-IR) spectra were recorded on American Nicolet FT-IR spectrometer (Nexus FT-IR 470) with KBr pellet technique and the range is 4000–400  $\text{cm}^{-1}$ . The morphologies and microstructures of the samples were observed on a JEOL JSM-6700F scanning electron microscopy (SEM). Transmission electron microscopy (TEM) and high-resolution transmission electron microscopy (HRTEM) images were obtained on a JEM-2010F electron microscope (JEOL, Japan) with an acceleration voltage of 200 kV. The specific surface areas and pore sizes were measured by a Quantachrome NOVA2000e instrument (USA). The specific surface areas and pore sizes of the samples were obtained using the Brunauer-Emmett-Teller (BET) and Barrett-Joyner-Halenda (BJH) methods, respectively. X-ray photoelectron spectroscopy (XPS) measurement was recorded in an Axis Ultra spectrometer with a monochromatized  $\text{Al-K}\alpha$  X-ray source (225 W). Survey and multi-region spectra were recorded at C 1s, N 1s, O 1s and Cu 2p photoelectron peaks. The optical diffuse reflectance spectra (UV-vis) were measured on a PerkinElmer Lambda 750 s UV-vis-NIR spectrometer equipped with an integrating sphere.  $\text{BaSO}_4$  was used as the reference material, and the polycrystalline samples were ground well before the measurement. The photoluminescence (PL) spectra of the samples were recorded on a Varian

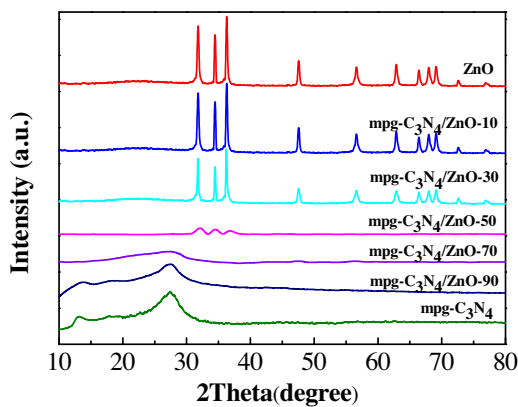


**Fig. 1.** XRD patterns of mpg-C<sub>3</sub>N<sub>4</sub>, ZnO, and the synthesized mpg-C<sub>3</sub>N<sub>4</sub>/ZnO nanocomposites.

Cary Eclipse spectrometer at an excitation wavelength of 375 nm. The photocurrent was measured on an electrochemical analyzer (CHI660B, Shanghai, China) using a typical three-electrode cell with a working electrode, a Pt counter electrode, and a standard calomel reference electrode. Na<sub>2</sub>SO<sub>4</sub> (0.5 mol L<sup>-1</sup>) aqueous solution was used as the electrolyte. The working electrode was prepared as the following process: 50 mg of the as-prepared photocatalyst was suspended in 0.5 mL of DMF, which was then dip-coated onto a 10 mm × 20 mm fluorine-doped tin oxide (FTO) glass electrode. The electrode was calcined at 350 °C for 1 h to eliminate the organic additives completely.

#### 2.4. Photocatalytic performance test

Photocatalytic activity of the mpg-C<sub>3</sub>N<sub>4</sub>/ZnO samples was evaluated by photocatalytic degradation of MO aqueous solution under visible-light irradiation. In each experiment, 50 mg of photocatalyst was added into 100 mL of MO solution (10 mg L<sup>-1</sup>). Before light irradiation, the suspensions were magnetically stirred in the dark for 30 min to ensure the adsorption-desorption equilibrium between MO molecules and the photocatalyst reaches. Then, a 350 W tungsten lamp with a cutoff filter ( $\lambda > 400$  nm) was used as the visible-light source. At 20 min intervals, a 4 mL solution was sampled and centrifuged to remove the photocatalyst particles, and its absorbance was detected using a UV-vis spectrometer at 464 nm. To estimate the photostability of the photocatalysts, the sample after one trial was collected through centrifugation, washed by deionized water and dried for the subsequent cycle test.

### 3. Results and discussion

#### 3.1. Characterization

##### 3.1.1. Structural information

Facile preparation of heterostructured mpg-C<sub>3</sub>N<sub>4</sub>/ZnO nanocomposite photocatalysts is realized by a calcination approach. The structural information of as-prepared mpg-C<sub>3</sub>N<sub>4</sub>/ZnO is provided by XRD, FT-IR and XPS measurements.

XRD analysis is used to investigate the phase structure of the mpg-C<sub>3</sub>N<sub>4</sub>/ZnO nanocomposite photocatalysts, and the graphitic stacking structure for all tested mpg-C<sub>3</sub>N<sub>4</sub>/ZnO materials is confirmed by the result shown in Fig. 1. As shown in Fig. 1, mpg-C<sub>3</sub>N<sub>4</sub> sample demonstrated the strongest peak at  $2\theta = 27.3^\circ$  corresponded to the (002) planes, typical interplanar stacking structures of graphitic materials [57,58]. According to the literature [57] that g-C<sub>3</sub>N<sub>4</sub> structure had a weak diffraction peak in the vicinity of  $2\theta = 13.2^\circ$ , attributed to the g-C<sub>3</sub>N<sub>4</sub> (100) crystal plane and in-plane

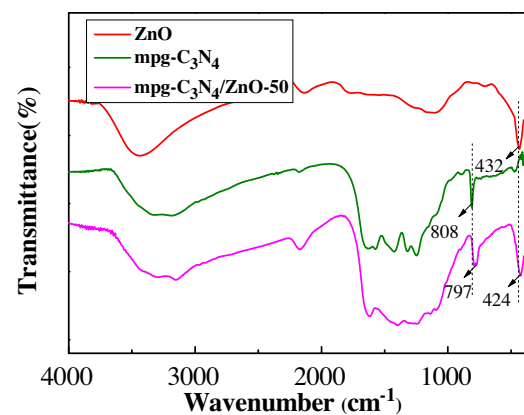


**Fig. 2.** FT-IR spectra of mpg-C<sub>3</sub>N<sub>4</sub>, ZnO, and the synthesized mpg-C<sub>3</sub>N<sub>4</sub>/ZnO samples.

structural packing motif. For the mpg-C<sub>3</sub>N<sub>4</sub> sample, this diffraction peak was broadened and weak, reflecting the effect of the geometric confinement in the nanosized pore walls. While pure ZnO presents the sharp diffractions of typical wurtzite hexagonal zinc oxide phase [59]. With respect to the mpg-C<sub>3</sub>N<sub>4</sub>/ZnO-x composites, the intensities of mpg-C<sub>3</sub>N<sub>4</sub> diffraction peaks weakened with the decrease of the weight ratio of dicyandiamide in the precursor mixtures and even disappeared when the content of mpg-C<sub>3</sub>N<sub>4</sub> in the composites decreased to 50%, while the peaks of ZnO appeared. The intensity of ZnO peaks enhanced with the further decrease of the content of mpg-C<sub>3</sub>N<sub>4</sub> and the increase of the ratio of ZnO. However, no typical patterns of mpg-C<sub>3</sub>N<sub>4</sub> (002) were observed in mpg-C<sub>3</sub>N<sub>4</sub>/ZnO composites with the high ZnO content (>50%), which was due to the low mpg-C<sub>3</sub>N<sub>4</sub> content in the samples. Therefore, in the XRD analysis, no impurity peaks were observed, which confirmed the high purity of the ZnO and C<sub>3</sub>N<sub>4</sub> products.

FT-IR spectra can provide plentiful structural information concerning about mpg-C<sub>3</sub>N<sub>4</sub>/ZnO nanocomposites (Fig. 2). In FT-IR spectrum of ZnO, the band at 432 cm<sup>-1</sup> is due to the Zn-O stretching mode, which indicates the formation of ZnO crystal [9]. For pure mpg-C<sub>3</sub>N<sub>4</sub>, a group of peaks appeared in the range from 1200 ~ 1700 cm<sup>-1</sup> attributed to the typical stretching vibration of CN heterocycles, while the sharp peak at 808 cm<sup>-1</sup> is attributed to the breathing vibration of triazine units, revealing that the local structure of the obtained mpg-C<sub>3</sub>N<sub>4</sub> is composed of triazine units [57,60]. The FT-IR spectrum of mpg-C<sub>3</sub>N<sub>4</sub>/ZnO-50 resembles mpg-C<sub>3</sub>N<sub>4</sub> in the characteristic bands, revealing the typical graphitic structure of carbon nitride was well reserved after homogeneous hybridization with ZnO, though the characteristic bands of graphitic C<sub>3</sub>N<sub>4</sub> red-shifted with the band strengths weakened, which indicates that the conjugated structures of mpg-C<sub>3</sub>N<sub>4</sub> are stretched and a more widely conjugated systems containing mpg-C<sub>3</sub>N<sub>4</sub> and ZnO have been generated [52].

The high-resolution XPS surface probe technique analysis of mpg-C<sub>3</sub>N<sub>4</sub>/ZnO-50 was conducted (Fig. 3), taken as being representative, to investigate the stoichiometric chemistry of the prepared composite catalysts. As shown in Fig. 3a, the peak at 287.8 eV can be attributed to the C 1s peak in the sample. The peak located at 397.9 eV is assigned to the N 1s peak. While the two peaks at 530.5 eV and 1021.8 eV were designated as the O 1s and Zn 2p, respectively, suggesting that the coexistence of elements C, N, Zn, and O in the sample. In Fig. 3b, we can see that C 1s spectrum can be deconvoluted into three components at about 284.6, 286.5, and 287.8 eV, respectively. The peak centered at 284.6 eV is ascribed to the adventitious hydrocarbon from the XPS instrument itself and sp<sup>2</sup>C atoms bonded to N in an aromatic ring (N=C=N), whereas the energy contribution at 286.5 eV is attributed to the sp<sup>3</sup> hybridized

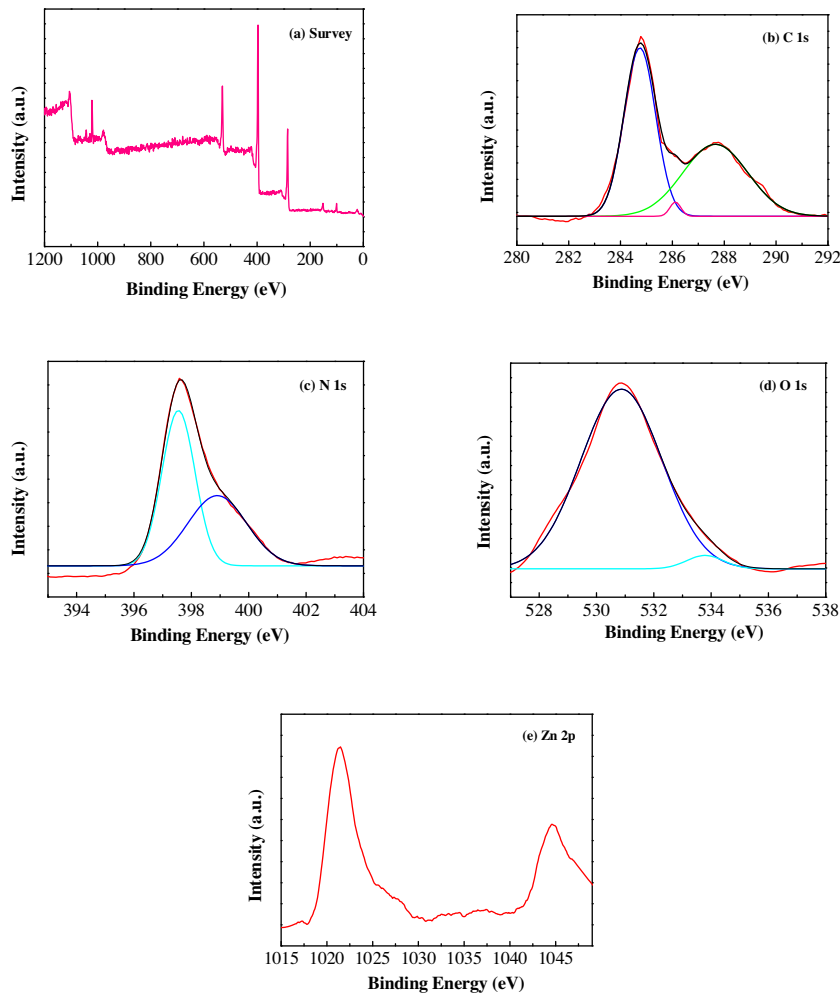


**Fig. 3.** XPS spectra of the synthesized mpg-C<sub>3</sub>N<sub>4</sub>/ZnO-50 sample: (a) Survey of the sample; (b) C 1s; (C) N 1s; (d) O 1s; (e) Zn 2p.

C atoms (C—(N)<sub>3</sub>). The peak situating at 287.8 eV can be assigned to the pure graphitic sites in a C—N—C coordination [61–63]. Fig. 3c shows the N 1s XPS spectrum can also be fitted into one main peak at 397.9 eV attributed to the aromatic N bonded to two carbon atoms (C=N=C), and a weak shoulder at 399.2 eV corresponded to either tertiary nitrogen N—(C)<sub>3</sub> groups linking structural motif (C<sub>6</sub>N<sub>7</sub>) or amino groups carrying hydrogen ((C)<sub>2</sub>—N—H) in connection with structural defects and incomplete condensation [64]. In the O 1s XPS spectrum (Fig. 3d), the main peak centered at 531.1 eV is assigned to O<sup>2-</sup> ions in the Zn—O bonding of the wurtzite ZnO structure [65] and the shoulder peak located at 533.8 eV is related to OH group absorbed onto the surface of the composite [66]. The Zn 2p XPS spectrum (Fig. 3e) contains a doublet at the binding energy of 1021.8 and 1044.7 eV, assigned to Zn 2p<sub>3/2</sub> and 2p<sub>1/2</sub> lines, respectively. The binding energy distance between these two lines is 22.9 eV, which is within the standard reference value of ZnO [67]. The binding energies and the binding energy difference indicate that the Zn ions in the composites are of +2 states.

### 3.1.2. Morphology

The SEM, TEM and HRTEM images of the ZnO, mpg-C<sub>3</sub>N<sub>4</sub>, and as-prepared mpg-C<sub>3</sub>N<sub>4</sub>/ZnO-50 sample are shown in Fig. 4. As displayed in Fig. 4a, the SEM image of mpg-C<sub>3</sub>N<sub>4</sub>, presenting a typical multilayer stacking structure of the graphitic nature of carbon nitride. Fig. 4b shows the pure ZnO sample is revealed to be mainly composed of non-uniformly aggregated globular particles with the average particle size of around 100 nm [68]. The mpg-C<sub>3</sub>N<sub>4</sub>/ZnO-50

sample exhibited the sheet-like morphology and the micron-sized sheets were stacked, which could be clearly observed in Fig. 4c. In addition, a large number of ZnO particles were clearly found on the surface of mpg-C<sub>3</sub>N<sub>4</sub> at high magnification. The microstructure was further investigated by TEM. Some floc-like mpg-C<sub>3</sub>N<sub>4</sub> with wormlike porous morphology appeared (Fig. 4d). It speculated that the template entered into the crystal lattice of g-C<sub>3</sub>N<sub>4</sub>, which probably changed its morphology. The pure ZnO mainly exhibited globular shape with the average particle size of around 100 nm (Fig. 4e). The TEM image of mpg-C<sub>3</sub>N<sub>4</sub>/ZnO-50 sample showed obvious layered structure (Fig. 4f). Coinciding with the SEM observation, it was concluded that the ultimate nanocomposites even after hybridization with ZnO were consisted of stacked graphitic planes constructed from the triazine building units. The TEM image revealed that almost no free ZnO nanoparticles were found outside of the mpg-C<sub>3</sub>N<sub>4</sub> sheet, indicating that ZnO nanoparticles were successfully deposited on the surface of the mpg-C<sub>3</sub>N<sub>4</sub> sheet. MPG-C<sub>3</sub>N<sub>4</sub> also prevented the agglomeration of ZnO nanoparticles. The HRTEM images of mpg-C<sub>3</sub>N<sub>4</sub>/ZnO-50 composite (Fig. 4g and h) clearly revealed a close interface between the mpg-C<sub>3</sub>N<sub>4</sub> and ZnO, indicating the formation of heterojunction. Fig. 4h shows that the ZnO nanoparticles uniformly hybridized with the layered mpg-C<sub>3</sub>N<sub>4</sub>. And an interplanar distance of 0.270 nm attributed to the (100) crystal plane of the wurtzite ZnO hexagonal phase was also observed.

The morphology studies revealed that mpg-C<sub>3</sub>N<sub>4</sub> with thin sheet like porous structures could serve as a support to bound ZnO

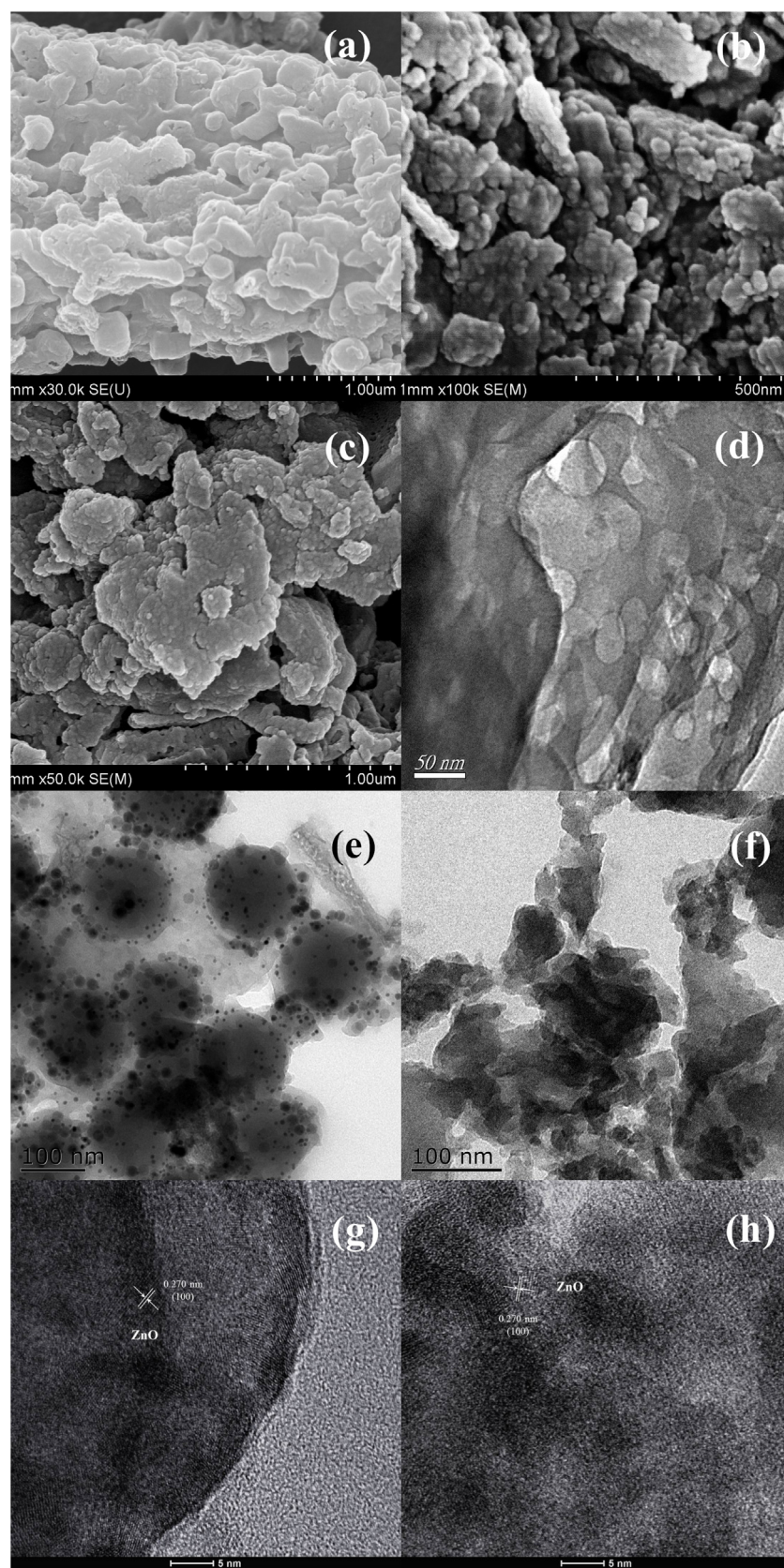


**Fig. 4.** SEM images of mpg-C<sub>3</sub>N<sub>4</sub> (a), ZnO (b), and mpg-C<sub>3</sub>N<sub>4</sub>/ZnO-50(c), TEM images of mpg-C<sub>3</sub>N<sub>4</sub> (d), ZnO (e), and the mpg-C<sub>3</sub>N<sub>4</sub>/ZnO-50 (f), and HRTEM images of mpg-C<sub>3</sub>N<sub>4</sub>/ZnO-50 (g), (h).

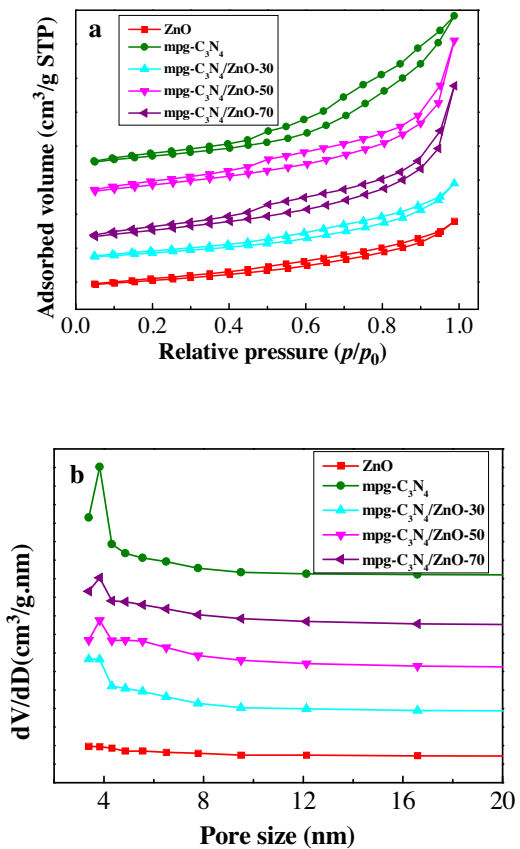


**Fig. 5.** Nitrogen adsorption-desorption isotherms (a) and BJH pore-size distribution curves (b) of mpg-C<sub>3</sub>N<sub>4</sub>, ZnO and mpg-C<sub>3</sub>N<sub>4</sub>/ZnO materials.

**Table 1**  
BET areas of the different samples.

samples	S <sub>BET</sub> (m <sup>2</sup> g <sup>-1</sup> )
ZnO	22.8
mpg-C <sub>3</sub> N <sub>4</sub> /ZnO-10	24.7
mpg-C <sub>3</sub> N <sub>4</sub> /ZnO-30	30.2
mpg-C <sub>3</sub> N <sub>4</sub> /ZnO-50	34.3
mpg-C <sub>3</sub> N <sub>4</sub> /ZnO-70	31.5
mpg-C <sub>3</sub> N <sub>4</sub> /ZnO-90	25.2
mpg-C <sub>3</sub> N <sub>4</sub>	36.3

particles in the hybrid system, which leads to the formation of interfaces between mpg-C<sub>3</sub>N<sub>4</sub> and ZnO and to favorable photogenerated charge transfer at the interface.

### 3.1.3. Textural property

The textural property of as-prepared mpg-C<sub>3</sub>N<sub>4</sub>/ZnO materials is characterized by nitrogen porosimetry measurement. The nitrogen adsorption-desorption isotherms and BJH pore-size distribution curves are shown in Fig. 5. BET surface areas and pore sizes are summarized in Table 1. We found from Fig. 5a that all mpg-C<sub>3</sub>N<sub>4</sub>/ZnO nanocomposites exhibited type IV isotherms with H3 hysteresis loops [69] at high relative pressure between 0.5 and 1.0, suggesting that the obtained samples have the mesoporous structures. Moreover, the type of H3 hysteresis loops is often observed on the aggregates of plate-like particles leading to slit-shaped pores which conformed to the nanosheet-like morphology (Fig. 4a and b). Clearly, as shown in Fig. 5b, the average pore sizes of all the samples distributed in the center of 5 nm, which is consistent with the size of the SBA-15 template [70], suggesting that the mesostructure is well-preserved after pyrolysis. Based on desorption curve, the BET surface area of mpg-C<sub>3</sub>N<sub>4</sub>/ZnO nanocomposites is lower

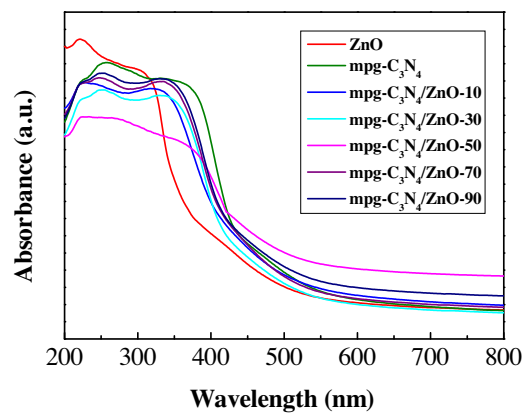


**Fig. 6.** UV-vis absorbance spectra of mpg-C<sub>3</sub>N<sub>4</sub>, ZnO, and the synthesized mpg-C<sub>3</sub>N<sub>4</sub>/ZnO nanocomposites.

than that of mpg-C<sub>3</sub>N<sub>4</sub> (36.3 m<sup>2</sup> g<sup>-1</sup>) but is higher than that of pure ZnO (22.8 m<sup>2</sup> g<sup>-1</sup>). The surface area of the composite photocatalyst increased with the reduction of the ZnO contents in the final composites and reached the maximum of 34.3 m<sup>2</sup> g<sup>-1</sup> for mpg-C<sub>3</sub>N<sub>4</sub>/ZnO-50. Further decreasing of the ZnO content led to a lower surface area of 25.2 m<sup>2</sup> g<sup>-1</sup> for mpg-C<sub>3</sub>N<sub>4</sub>/ZnO-90.

### 3.1.4. Optical absorption property

The photoabsorption behaviors of the prepared mpg-C<sub>3</sub>N<sub>4</sub>/ZnO composite photocatalysts were studied by UV-vis diffuse reflectance spectra (DRS), and the result is shown in Fig. 6. The obvious red shift of the absorption may result in the enhanced photocatalytic properties in the visible region. The pure ZnO has strong absorption in the UV region wavelength threshold of 388 nm, corresponding to the band gap of 3.20 eV. Distinct from the ZnO absorption behavior, the absorption offset of mpg-C<sub>3</sub>N<sub>4</sub> occurs at 460 nm, giving the band gap of 2.70 eV, which indicated its visible-light-induced photocatalytic activity [36]. Noticeably, the absorption edges of the mpg-C<sub>3</sub>N<sub>4</sub>/ZnO-x composites shifted significantly to the longer wavelength region in comparison with that of pure ZnO and mpg-C<sub>3</sub>N<sub>4</sub>, obviously demonstrating that the absorption edges of the composites moved to lower energy region. The mpg-C<sub>3</sub>N<sub>4</sub>/ZnO-50 composite shows broad and strengthened absorption in the visible light range among five tested mpg-C<sub>3</sub>N<sub>4</sub>/ZnO materials. These results may be attributed to the synergistic effect between mpg-C<sub>3</sub>N<sub>4</sub> and ZnO in the composite samples [69]. The enhanced light adsorption of the composites can make the utmost of visible light and thus result in the production of more electron-hole pairs under visible light illumination, which subsequently led to a higher photocatalytic activity.

## 3.2. Photocatalytic studies

### 3.2.1. Visible-light photocatalytic activity

Fig. 7 depicts the photocatalytic activities for the decomposition of MO on pure ZnO, mpg-C<sub>3</sub>N<sub>4</sub>, and the as-prepared mpg-C<sub>3</sub>N<sub>4</sub>/ZnO-x nanocomposite photocatalysts under visible light illumination. Without the presence of a catalyst, the degradation of MO was negligible under visible-light irradiation, indicating the high stability of MO under visible-light irradiation. To disclose the adsorption effect of the catalyst on MO, the suspension was stirred for 30 min in the dark to achieve adsorption-desorption equilibrium before the photodegradation test. The initial concentration of the MO suspension was measured and used as the initial concentration C<sub>0</sub>. The Y axis is reported as C/C<sub>0</sub>, where C is the actual concentration of MO at the indicated reaction time. As can be clearly seen in Fig. 7, the pure ZnO played limited role in degrading MO

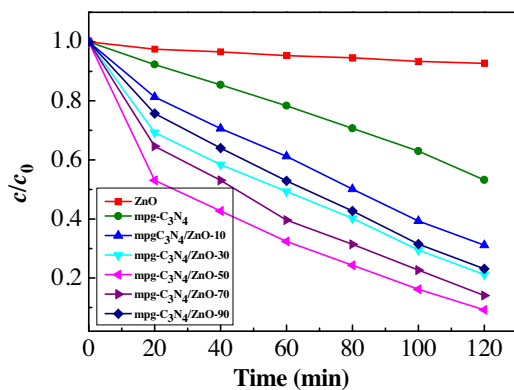


**Fig. 7.** Effect of various photocatalysts including pure ZnO, mpg-C<sub>3</sub>N<sub>4</sub> and mpg-C<sub>3</sub>N<sub>4</sub> nanocomposites on degradation efficiency of MO under visible light (light Source: 350 W of tungsten lamp; catalyst dose: 0.05 g; reaction time: 120 min; [MO] initial: 10 mg L<sup>-1</sup>; volume 100 mL; 400 nm <  $\lambda$  < 680 nm).

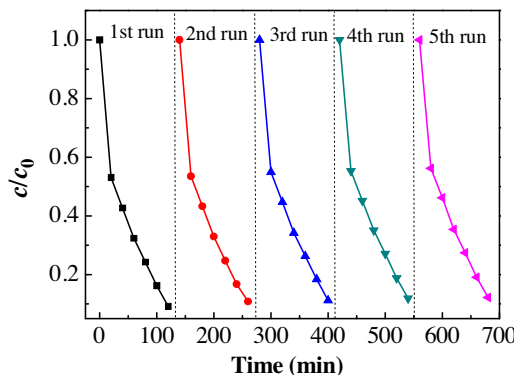


**Fig. 8.** Recycling experiments of visible-light photocatalytic degradation of MO over the mpg-C<sub>3</sub>N<sub>4</sub>/ZnO-50 (light Source: 350 W of tungsten lamp; catalyst dose: 0.05 g; reaction time: 120 min; [MO] initial: 10 mg L<sup>-1</sup>; volume 100 mL; 400 nm <  $\lambda$  < 680 nm).

due to the large band gap energy, giving photocatalytic efficiency of 7.3%. Mpg-C<sub>3</sub>N<sub>4</sub> has a better performance in photodegradation than ZnO, showing degradation efficiency of 46.8% after 2 h of irradiation, due to the absorption in the visible light region. The decrease in the concentration of MO is faster and more prominent with mpg-C<sub>3</sub>N<sub>4</sub>/ZnO nanocomposites than with pure mpg-C<sub>3</sub>N<sub>4</sub> or ZnO under the same experimental conditions. The photocatalytic activities of the mpg-C<sub>3</sub>N<sub>4</sub>/ZnO nanocomposites increased with the increase of the ZnO proportion in the composites first and then decreased. Mpg-C<sub>3</sub>N<sub>4</sub>/ZnO-50 exhibited the highest photocatalytic activity with the photodegradation efficiency of 90.8%. It is believed that excess ZnO bulks might act as electron-hole recombination sites and suppress the photoinduced charge transfer. The enhanced photocatalytic performance of the mpg-C<sub>3</sub>N<sub>4</sub>/ZnO nanocomposite may be attributed to the synergistic effect between the interface of mpg-C<sub>3</sub>N<sub>4</sub> and ZnO.

### 3.2.2. Regeneration and reusability

Regeneration and reusability of the mpg-C<sub>3</sub>N<sub>4</sub>/ZnO-50 nanocomposite was evaluated for MO degradation under visible light irradiation. The mpg-C<sub>3</sub>N<sub>4</sub>/ZnO-50 nanocomposite was reused for the five runs and the results were displayed in Fig. 8. For each recycling run, mpg-C<sub>3</sub>N<sub>4</sub>/ZnO-50 is collected by centrifugation, and then washed with deionized water for three times and dried. As shown in Fig. 8, mpg-C<sub>3</sub>N<sub>4</sub>/ZnO-50 retained over 88% of its original photocatalytic activity after five recycling experimental runs. The small loss might result from the loss of

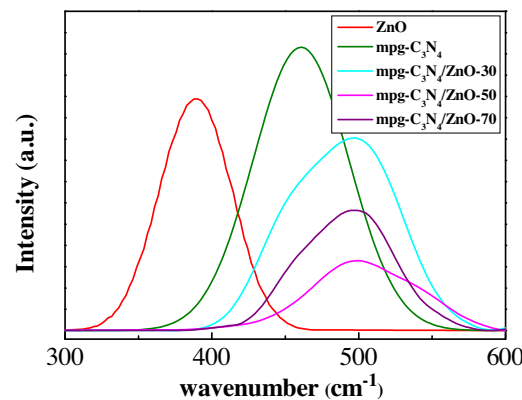


**Fig. 9.** Photoluminescence emission spectra of mpg-C<sub>3</sub>N<sub>4</sub>, ZnO, and the synthesized mpg-C<sub>3</sub>N<sub>4</sub>/ZnO samples.

photocatalyst during recycling. Accordingly, the homogeneous hybridization between ZnO and mpg-C<sub>3</sub>N<sub>4</sub> could prohibit the consumption of ZnO and enhance the activity and stability of the mpg-C<sub>3</sub>N<sub>4</sub>/ZnO nanocomposite photocatalysts, promising as visible-light-driven photocatalysts to practical applications of environmental protection.

### 3.3. Mechanism considerations

#### 3.3.1. Photoluminescence measurements

In order to investigate the influence of the synergy of doped ZnO with mpg-C<sub>3</sub>N<sub>4</sub> nanosheets on the photocatalytic activity, photoluminescence (PL) spectroscopy studies were performed, through which the photogenerated recombination of e<sub>CB</sub><sup>-</sup>-h<sub>VB</sub><sup>+</sup> pairs on each mpg-C<sub>3</sub>N<sub>4</sub>/ZnO nanocomposite sample could be found out. Fig. 9 shows the room temperature PL spectra of ZnO, mpg-C<sub>3</sub>N<sub>4</sub>, and mpg-C<sub>3</sub>N<sub>4</sub>/ZnO under the excitation wavelength of 231 nm and the emission spectra were recorded in a range between 300 and 600 nm. It is well-known that the recombination of electron-hole pairs within the semiconductor can release energy in the form of PL emission. In general, a lower PL intensity indicates lower recombination of charge carriers, leading to higher photocatalytic activity. It is clear that the PL spectra of mpg-C<sub>3</sub>N<sub>4</sub> have a strong emission peak at around 460 nm, which is consistent with the UV-vis results (Fig. 6) and literature reported value [71]. For pure ZnO, the emission intensity was lower than that of mpg-C<sub>3</sub>N<sub>4</sub> at similar emission position. The PL emission of mpg-C<sub>3</sub>N<sub>4</sub>/ZnO nanocomposite was significantly quenched with a red-shifted emission peak at the region of 500–580 nm, as compared with mpg-C<sub>3</sub>N<sub>4</sub>. Furthermore, the PL spectra of mpg-C<sub>3</sub>N<sub>4</sub>/ZnO nanocomposite were similar to mpg-C<sub>3</sub>N<sub>4</sub>, but its peak intensity obviously decreased. In particular, the PL peak of mpg-C<sub>3</sub>N<sub>4</sub>/ZnO-50 nanocomposite exhibited the lowest intensity, which is well consistent with the result of the photocatalytic activity (Fig. 7). On the basis of these results, it concluded that in the case of mpg-C<sub>3</sub>N<sub>4</sub>/ZnO-50 nanocomposite, the photogenerated electron-hole pairs can efficiently transfer at the interface of heterostructure, resulting in the highest photocatalytic activity under visible light irradiation.

#### 3.3.2. Photoelectrochemical experiment

It is well-known that the photocatalytic redox reactions are intimately relevant to the separation, migration and capture of photoinduced electrons and holes arisen from the excited semiconductor photocatalysts. To qualitatively investigate the separation efficiency of photoinduced charges during the photocatalytic reactions, the photocurrent responses were carried out for the ZnO, mpg-C<sub>3</sub>N<sub>4</sub>, and mpg-C<sub>3</sub>N<sub>4</sub>/ZnO-50 nanocomposites under visible

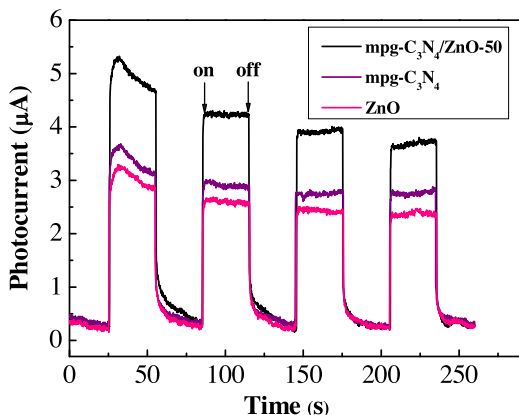


**Fig. 10.** Transient photocurrent response of mpg-C<sub>3</sub>N<sub>4</sub>, ZnO and the synthesized mpg-C<sub>3</sub>N<sub>4</sub>/ZnO-50 sample electrodes in 0.5 mol L<sup>-1</sup> Na<sub>2</sub>SO<sub>4</sub> aqueous solution under visible light irradiation ( $\lambda > 400$  nm).

light irradiation. Fig. 10 shows the photocurrent-time (*I-t*) curves for the three samples with on-off cycles of intermittent irradiation. As shown in Fig. 10, the photocurrent value rapidly decreased to zero as soon as the irradiation of light turned off, and the photocurrent came back to a constant value when the light was on again, which was reproducible. This indicated that most of photo-generated electrons were transported to the surface of the samples to produce photocurrent under visible-light irradiation. After the equilibration of separation and recombination of electron-hole pairs, the photocurrent reached a steady value [72,73]. Because of the large band gap, pure ZnO electrode had the weakest response under visible light illumination. The mpg-C<sub>3</sub>N<sub>4</sub>/ZnO-50 composite sample had higher photocurrent intensity than pure ZnO and mpg-C<sub>3</sub>N<sub>4</sub>. This result indicated that more efficient separation and transportation of the photogenerated electrons and holes were realized, which could be ascribed to the heterojunction built between mpg-C<sub>3</sub>N<sub>4</sub> and ZnO. The result was consistent with that of PL measurement.

### 3.3.3. Free radical and hole scavenging experiments

In order to understand the mechanism on the enhanced photocatalytic activity of the mpg-C<sub>3</sub>N<sub>4</sub>/ZnO nanocomposite photocatalyst in depth, the active species generated during the process of mpg-C<sub>3</sub>N<sub>4</sub>/ZnO-photocatalyzed MO degradation are identified by free radical and hole trapping experiments. In this study, to investigate the role of these reactive species in the mpg-C<sub>3</sub>N<sub>4</sub>-ZnO system, *tert*-butyl alcohol (t-BuOH), EDTA and 1, 4-benzoquinone (BQ) are used as the hydroxyl radical (·OH) scavenger, hole (h<sub>VB</sub><sup>+</sup>) scavenger and superoxide radical (·O<sub>2</sub><sup>-</sup>) scavenger, respectively [74].

Fig. 11 displays the influence of various scavengers on the visible-light photocatalytic activity of mpg-C<sub>3</sub>N<sub>4</sub>/ZnO (represented by mpg-C<sub>3</sub>N<sub>4</sub>/ZnO-50) toward the degradation of MO. It can be seen that when BQ was conducted as an ·O<sub>2</sub><sup>-</sup> scavenger, a dramatic change in the photocatalytic activity was observed compared with the absence of scavenger, confirming that the dissolved O<sub>2</sub> has a clear effect on the photodegradation process under visible-light irradiation. Meanwhile, a similar change in the photocatalytic activity was observed upon the addition of t-BuOH as an ·OH scavenger. Nevertheless, the photodegradation of MO over the mpg-C<sub>3</sub>N<sub>4</sub>/ZnO can also be suppressed after the addition of EDTA as a hole (h<sub>VB</sub><sup>+</sup>) scavenger compared with no scavenger under similar conditions. The above result indicates that h<sub>VB</sub><sup>+</sup> is also the active species generated in the mpg-C<sub>3</sub>N<sub>4</sub>/ZnO photocatalytic system besides ·O<sub>2</sub><sup>-</sup> and ·OH radical in the mpg-C<sub>3</sub>N<sub>4</sub>-ZnO system.

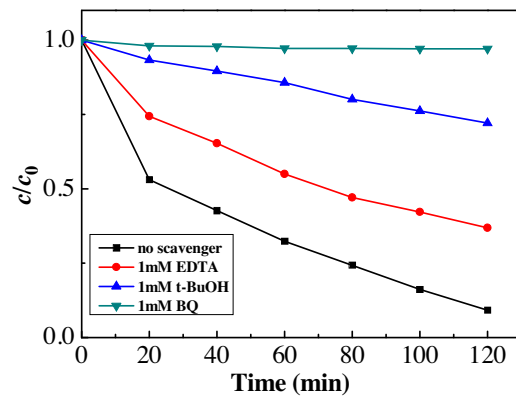
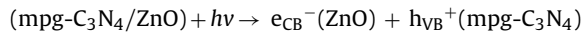


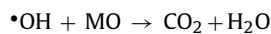
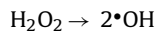
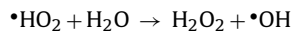
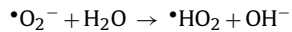
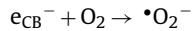
**Fig. 11.** Influence of various scavengers on the visible-light photocatalytic activity of mpg-C<sub>3</sub>N<sub>4</sub>/ZnO-50 toward the degradation of MO. (light Source: 350 W of tungsten lamp; catalyst dose: 0.05 g; reaction time: 120 min; [MO]<sub>initial</sub>: 10 mg L<sup>-1</sup>; volume 100 mL; 400 nm < λ < 680 nm).

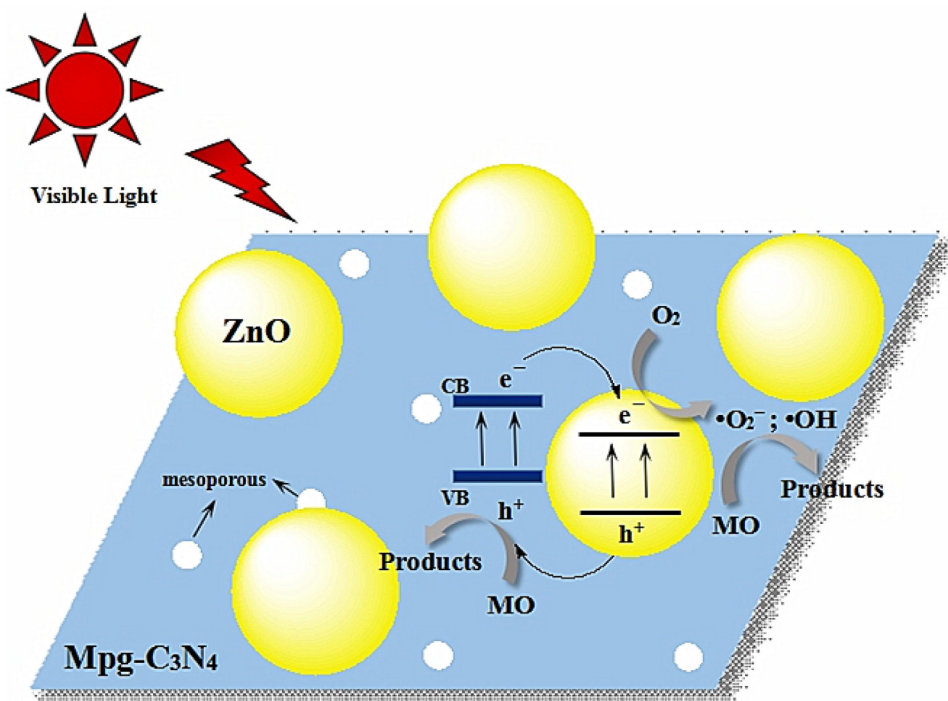
### 3.3.4. Mechanism analysis

On the basis of the related literature work and the above experimental results including physicochemical properties, photocatalytic properties as well as the identified active species, a possible photocatalytic mechanism of the as prepared mpg-C<sub>3</sub>N<sub>4</sub>/ZnO nanocomposites under visible light irradiation was tentatively proposed. As well known, ZnO and mpg-C<sub>3</sub>N<sub>4</sub> are both typical n-type semiconductors. In the subsequent process of calcination, mpg-C<sub>3</sub>N<sub>4</sub> combined with ZnO nanoparticles by sintering. Therefore, at the interface between mpg-C<sub>3</sub>N<sub>4</sub> and ZnO nanoparticle, an n-n heterojunction will be formed. Under visible light irradiation, mpg-C<sub>3</sub>N<sub>4</sub>/ZnO composites can be excited to generate electrons and holes and the excited electrons transfer from the conduction band (CB) of mpg-C<sub>3</sub>N<sub>4</sub> to the conduction band (CB) of ZnO. The enhancement of photocatalytic performance of the composite photocatalysts was mainly attributed to the effective photo-excited electron and hole separation at the heterojunction interfaces [68]. Since the CB edge potential of mpg-C<sub>3</sub>N<sub>4</sub> is more negative than that of ZnO, the excited electrons in mpg-C<sub>3</sub>N<sub>4</sub> transferred to the CB of ZnO [75,76]. Reversely, the holes from the VB of ZnO were injected to that of mpg-C<sub>3</sub>N<sub>4</sub>. Accordingly, an internal electrostatic potential was formed in the space charge region, which was propitious to the separation of the photogenerated charge carriers. The charges would subsequently transform to the surface of the composite semiconductor to react with water and dissolved oxygen to generate superoxide and hydroxyl radicals or interact with MO directly. The radicals were able to oxidize the organics owing to their high oxidative capacity, producing visible light photocatalytic activity. The photocatalytic mechanism in our experiment was proposed as follows:



Electrospun nanofibers of mpg-C<sub>3</sub>N<sub>4</sub>/ZnO heterojunction





**Scheme 1.** A possible visible-light photocatalytic degradation diagram of mpg-C<sub>3</sub>N<sub>4</sub>/ZnO nanocomposite.

Based on the above discussions, it can be concluded that the significant improvement of photocatalytic activities for the mpg-C<sub>3</sub>N<sub>4</sub>/ZnO nanocomposite semiconductors can be ascribed not only to the improved optical absorption property arising from the heterojunction structure between mpg-C<sub>3</sub>N<sub>4</sub> and ZnO, but also to their synergetic effects of the inner electric field and matched energy band structure that bring the high separation rate of the photogenerated charge carriers (**Scheme 1**).

#### 4. Conclusions

In this paper, a series of highly efficient visible-light-driven mpg-C<sub>3</sub>N<sub>4</sub>/ZnO nanocomposite photocatalysts were successfully synthesized by a facile one-step calcination approach. The photodegradation of MO experiments together with the PL analysis revealed that the mpg-C<sub>3</sub>N<sub>4</sub>/ZnO nanocomposite showed a significant effect on the separation of photogenerated charge carriers as well as the visible light photocatalytic activity. The mpg-C<sub>3</sub>N<sub>4</sub>/ZnO-50 nanocomposite degraded nearly 50% of MO within 4 min, and ~90% after 30 min. In addition, the prepared photocatalysts had relative stability under visible light irradiation. The enhanced photocatalytic activity of the mpg-C<sub>3</sub>N<sub>4</sub>/ZnO nanocomposites was mainly attributed to the synergetic effects between mpg-C<sub>3</sub>N<sub>4</sub> and ZnO. The results provided here not only offer a highly efficient and stable photocatalytic material for environmental remediation and solar utilization, but also shed a new insight and the easy preparation procedure for fabricating efficient heterostructured photocatalysts.

#### Acknowledgments

Financial support from Project supported by the National Natural Science Foundation of China (51572115) and Project supported by the Graduate Science Research Innovation Program Foundation of the Jiangsu Higher Education Institution of China (KYLX15\_1040) are gratefully acknowledged.

#### References

- [1] I.K. Konstantinou, T.A. Albanis, *Appl. Catal. B: Environ.* 42 (2003) 319–335.
- [2] D. Chatterjee, S. Dasgupta, *J. Photochem. Photobiol. C* 6 (2005) 186–205.
- [3] T. Tachikawa, M. Fujitsuka, T. Majima, *J. Phys. Chem. C* 111 (2007) 5259–5275.
- [4] K. Lv, Q. Xiang, J. Yu, *Appl. Catal. B: Environ.* 104 (2011) 275–281.
- [5] Q. Xiang, J. Yu, M. Jaroniec, *Nanoscale* 3 (2011) 3670–3678.
- [6] R. Asahi, T. Morikawa, T. Ohwaki, K. Aoki, Y. Taga, *Science* 293 (2001) 269–271.
- [7] H. Lachheb, E. Puzenat, A. Houas, M. Ksibi, E. Elaloui, C. Guillard, J.M. Herrmann, *Appl. Catal. B: Environ.* 39 (2002) 75–90.
- [8] G.K. Prasad, P.V.R.K. Ramacharyulu, B. Singh, K. Batra, A.R. Srivastava, K. Ganeshan, R. Vijayaraghavan, *J. Mol. Catal. A* 349 (2011) 55–62.
- [9] M. Samadie, H.A. Shivaeea, M. Zanettib, A. Pourjavadic, A. Moshfegh, *J. Mol. Catal. A* 359 (2012) 42–48.
- [10] Q. Xiong, M. Zhou, X. Qian, *Adv. Mater. Res.* 472–475 (2012) 3441–3444.
- [11] Y. Chen, C. Zhang, W. Huang, Y. Situ, H. Huang, *Mater. Lett.* 141 (2015) 294–297.
- [12] W. He, H. Zhao, H. Jia, J.J. Yin, Z. Zheng, *Mater. Res. Bull.* 53 (2014) 246–250.
- [13] S. Livraghi, A.M. Czoska, M.C. Paganini, E. Gimello, *J. Solid State Chem.* 182 (2009) 160–164.
- [14] X. Zhou, F. Peng, H. Wang, H. Yu, J. Yang, *Mater. Res. Bull.* 46 (2011) 840–844.
- [15] D. Zhang, F. Zeng, *Appl. Surf. Sci.* 257 (2010) 867–871.
- [16] L.G. Devi, S.G. Kumar, *Appl. Surf. Sci.* 261 (2012) 137–146.
- [17] L.G. Devi, K.E. Rajashekhar, *J. Mol. Catal. A* 334 (2011) 65–76.
- [18] G.S. Shao, F.Y. Wang, T.Z. Ren, Y. Liu, Z.Y. Yuan, *Appl. Catal. B* 92 (2009) 61–67.
- [19] C. Chen, W. Cai, M. Long, J. Zhang, B. Zhou, Y. Wu, D. Wu, *J. Hazard. Mater.* 178 (2010) 560–565.
- [20] J. Xu, Y. Ao, D. Fu, *Appl. Surf. Sci.* 256 (2009) 884–888.
- [21] F. Dong, H. Wang, G. Sen, Z. Wu, S.C. Lee, J. Hazard. Mater. 187 (2011) 509–516.
- [22] A. Charanpahari, S.S. Umare, S.P. Gokhale, V. Sudarsan, B. Sreedhar, R. Sasikal, *Appl. Catal. A* 443–444 (2012) 96–102.
- [23] E.A. Kozlova, T.P. Lyubina, M.A. Nasalevich, A.V. Vorontsov, A.V. Miller, V.V. Kaichev, V.N. Parmon, *Catal. Commun.* 12 (2011) 597–601.
- [24] S. Zhang, F. Peng, H. Wang, H. Yu, S. Zhang, J. Yang, H. Zhao, *Catal. Commun.* 12 (2011) 689–693.
- [25] V. Subramanian, E.E. Wolf, P.V. Kamat, *J. Am. Chem. Soc.* 126 (2004) 4943–4950.
- [26] A.Z. Jurek, E. Kowalska, J.W. Sobczak, W. Lisowski, B. Ohtani, A. Zaleska, *Appl. Catal. B* 101 (2011) 504–514.
- [27] S. Yin, T. Sato, *J. Photochem. Photobiol. A* 169 (2005) 89–94.
- [28] N. Wang, L. Zhu, K. Deng, Y. She, Y. Yu, H. Tang, *Appl. Catal. B: Environ.* 95 (2010) 400–407.
- [29] N. Fu, G. Lu, *Chem. Commun.* 24 (2009) 3591–3593.
- [30] S. Kim, J. Yeo, W. Choi, *Appl. Catal. B: Environ.* 84 (2008) 148–155.
- [31] N. Yang, G. Li, W. Wang, X. Yang, W.F. Zhang, *J. Phys. Chem. Solids* 72 (2011) 1319–1324.
- [32] J. Liu, R. Han, Y. Zhao, H. Wang, W. Lu, T. Yu, Y. Zhang, *J. Phys. Chem. C* 115 (2011) 4507–4515.

[33] K.S. Ahn, Y. Yan, S. Shet, T. Deutsch, J. Turner, M. Al-Jassim, *Appl. Phys. Lett.* 91 (2007) 1–3.

[34] X.Y. Yang, A. Wolcott, G. Wang, A. Sobo, R.C. Fitzmorris, F. Qian, J.Z. Zhang, Y. Li, *Nano Lett.* 9 (2009) 2331–2336.

[35] Y. Cui, Z. Ding, X. Fu, X. Wang, *Angew. Chem. Int. Ed.* 51 (2012) 11814–11818.

[36] X.C. Wang, K. Maeda, A. Thomas1, K. Takanabe, G. Xin, J.M. Carlsson, K. Domen, M. Antonietti, *Nat. Mater.* 8 (2009) 76–80.

[37] Q.J. Xiang, J.G. Yu, M. Jaroniec, *J. Phys. Chem. C* 115 (2011) 7355–7363.

[38] J.G. Yu, S.H. Wang, B. Cheng, Z. Lin, F. Huang, *Catal. Sci. Technol.* 3 (2013) 1782–1789.

[39] G.H. Dong, L.Z. Zhang, *J. Mater. Chem.* 22 (2012) 1160–1166.

[40] J. Mao, T. Peng, X. Zhang, K. Li, L. Ye, L. Zan, *Catal. Sci. Technol.* 3 (2013) 1253–1260.

[41] L. Ge, C.C. Han, J. Liu, Y.F. Li, *Appl. Catal. A* 409–410 (2011) 215–222.

[42] S.C. Yan, Z.S. Li, Z.G. Zou, *Langmuir* 25 (2009) 10397–10401.

[43] X. Jin, V.V. Balasubramanian, S.T. Selvan, D.P. Sawant, M.A. Chari, G.Q. Lu, A. Vinu, *Angew. Chem. Int. Ed.* 48 (2009) 7884–7887.

[44] E.Z. Lee, Y.S. Jun, W.H. Hong, A. Thomas, M.M. Jin, *Angew. Chem. Int. Ed.* 49 (2010) 9706–9710.

[45] J. Liang, Y. Zheng, J. Chen, J. Liu, D.H. Jurcakova, M. Jaroniec, S.Z. Qiao, *Angew. Chem.* 51 (2012) 3892–3896.

[46] Y.J. Cui, J.S. Zhang, G.G. Zhang, J.H. Huang, P. Liu, M. Antonietti, X.C. Wang, *J. Mater. Chem.* 21 (2011) 13032–13039.

[47] K. Takanabe, K. Kamata, X.C. Wang, M. Antonietti, J. Kubotaa, K. Domen, *PCCP* 12 (2010) 13020–13025.

[48] X.C. Wang, K. Maeda, X.F. Chen, K. Takanabe, K. Domen, Y.D. Hou, X.Z. Fu, M. Antonietti, *J. Am. Chem. Soc.* 131 (2009) 1680–1681.

[49] Y. Wang, J.S. Zhang, X.C. Wang, M. Antonietti, H. Li, *Angew. Chem.* 49 (2010) 3356–3359.

[50] J. Zhang, M. Zhang, R.Q. Sun, X. Wang, *Angew. Chem. Int. Ed.* 51 (2012) 10145–10149.

[51] Y. Wang, X.C. Wang, M. Antonietti, *Angew. Chem. Int. Ed.* 51 (2012) 68–89.

[52] Y.J. Wang, R. Shi, J. Lin, Y.F. Zhu, *Energy Environ. Sci.* 4 (2011) 2922–2929.

[53] W. Liu, M.L. Wang, C.X. Xu, S.F. Chen, X.L. Fu, *J. Mol. Catal. A: Chem.* 368 (2013) 9–15.

[54] D.M. Chen, K.W. Wang, D.G. Xiang, R.L. Zong, W.Q. Yao, Y.F. Zhu, *Appl. Catal. B: Environ.* 147 (2014) 554–561.

[55] D.M. Chen, K.W. Wang, T.Z. Ren, H. Ding, Y.F. Zhu, *Dalton Trans.* 43 (2014) 13105–13114.

[56] S.K. Le, T.S. Jiang, Q. Zhao, X.F. Liu, Y.Y. Li, B.W. Fang, M. Gong, *RSC Adv.* 6 (2016) 38811–38819.

[57] J.H. Liu, T. Zhang, Z.C. Wang, G. Dawson, W. Chen, *J. Mater. Chem.* 21 (2011) 14398–14401.

[58] F. Goettmann, A. Fischer, M. Antonietti, A. Thomas, *Angew. Chem. Int. Ed.* 45 (2006) 4467–4471.

[59] J. Singh, M.S.L. Hudson, S.K. Pandey, R.S. Tiwari, O.N. Srivastava, *Int. J. Hydrogen Energy* 37 (2012) 3748–3754.

[60] P. Niu, G. Liu, H.M. Cheng, *J. Phys. Chem. C* 116 (2012) 11013–11018.

[61] H.J. Yan, *Chem. Commun.* 48 (2012) 3430–3432.

[62] B. Chai, T.Y. Peng, J. Mao, K. Li, L. Zan, *PCCP* 14 (2012) 16745–16752.

[63] L. Ge, C.C. Han, *Appl. Catal. B* 117 (2012) 268–274.

[64] Q.J. Xiang, J.G. Yu, M. Jaroniec, *J. Phys. Chem. C* 115 (2011) 7355–7363.

[65] K. Kotisis, V. Staemmler, *Phys. Chem. Chem. Phys.* 8 (2006) 1490–1498.

[66] H.H. Ji, F. Chang, X.F. Hua, W. Qin, J.W. Shen, *J. Chem. Eng.* 218 (2013) 183–190.

[67] D.K. Mishra, J. Mohapatra, M.K. Sharma, R. Chattarjee, S.K. Singh, S. Varma, S.N. Behera, S.K. Nayak, P. Entel, *J. Magn. Magn. Mater.* 329 (2013) 146–152.

[68] Y.P. Zhu, M. Li, Y.L. Liu, T.Z. Ren, Z.Y. Yuan, *J. Phys. Chem. C* 118 (2014) 10963–10971.

[69] Y.F. Zhang, X.J. Bo, A. Nsabimana, C. Luhana, G. Wang, H. Wang, M. Li, L.P. Guo, *Biosens. Bioelectron.* 53 (2014) 250–256.

[70] X.S. Zhou, B. Jin, R.Q. Chen, F. Peng, Y.P. Fang, *Mater. Res. Bull.* 48 (2013) 1447–1452.

[71] Z. Ding, X. Chen, M. Antonietti, X. Wang, *ChemSusChem* 4 (2011) 274–281.

[72] J.G. Yu, B. Wang, *Appl. Catal. B: Environ.* 94 (2010) 295–302.

[73] Y.Y. Bu, Z.Y. Chen, W.B. Li, *Appl. Catal. B: Environ.* 144 (2014) 622–630.

[74] C.S. Pan, Y.F. Zhu, *Environ. Sci. Technol.* 44 (2010) 5570–5574.

[75] S.T. Kochuveedu, Y.H. Jang, Y.J. Jang, D.H. Kim, *J. Mater. Chem. A* 1 (2013) 898–905.

[76] G. Liu, P. Niu, C.H. Sun, S.C. Smith, Z.G. Chen, G.Q. Lu, H.M. Cheng, *J. Am. Chem. Soc.* 132 (2010) 11642–11648.